

pubs.acs.org/JACS Article

Transient Catenation in a Zirconium-Based Metal—Organic Framework and Its Effect on Mechanical Stability and Sorption Properties

- ⁴ Lee Robison, Xinyi Gong, Austin M. Evans, Florencia A. Son, Xingjie Wang, Louis R. Redfern,
- 5 Megan C. Wasson, Zoha H. Syed, Zhijie Chen, Karam B. Idrees, Timur Islamoglu,
- 6 Massimiliano Delferro, William R. Dichtel, François-Xavier Coudert, Nathan C. Gianneschi,*
- 7 and Omar K. Farha*

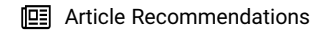


Cite This: https://dx.doi.org/10.1021/jacs.0c11266



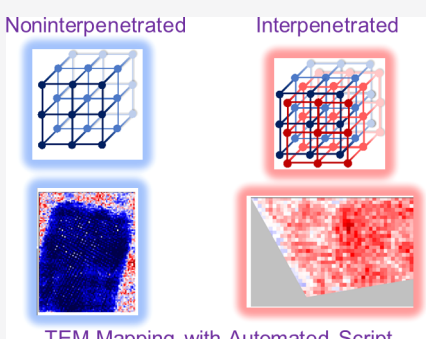
ACCESS I

III Metrics & More



s Supporting Information

8 **ABSTRACT:** Interpenetration of two or more sublattices is common among many 9 metal—organic frameworks (MOFs). However, interpenetration in zirconium cluster10 based MOFs is rarely observed. Herein, we study the evolution of one zirconium cluster11 based, 3,8-connected MOF from its non-interpenetrated (NU-1200) to interpenetrated (STA-26) isomer. We observe this transient catenation process indirectly using 13 ensemble methods, such as nitrogen porosimetry and X-ray diffraction, and directly, 14 using high-resolution transmission electron microscopy. The approach detailed here will 15 serve as a template for other researchers to monitor the interpenetration of their MOF 16 samples at the bulk and single-particle limits. We investigate the mechanical stability of 17 both lattices experimentally by pressurized *in situ* X-ray diffraction and nanoindentation 18 as well as computationally with density functional theory calculations. Both lines of 19 study reveal that STA-26 is considerably more mechanically stable than NU-1200. We 20 conclude this study by demonstrating the potential of these MOFs and their mixed



TEM Mapping with Automated Script

21 phases for the capture of gaseous n-hexane, used as a structural mimic for the chemical warfare agent sulfur mustard gas.

INTRODUCTION

23 Metal—organic frameworks (MOFs) are hybrid materials 24 obtained by the self-assembly of inorganic nodes and organic 25 linkers into periodic multidimensional structures with high 26 surface areas and porosities. 1,2 Among the thousands of MOFs 27 synthesized to date, zirconium cluster-based MOFs are 28 particularly robust due to the strength of the $\rm Zr(IV)-29$ carboxylate bond. $^{3-5}$ As such, Zr-based MOFs have been 30 explored for applications that may require demanding 31 conditions such as catalysis, 6,7 water sorption, $^{8-10}$ and gas 32 separations. 11,12

Interpenetration is defined by the presence of two or more mechanically interlocked periodic networks where, although no chemical bonds exist between the frameworks, disentanglement can only be achieved by breaking chemical bonds (Figure 1). Interpenetration typically enhances the stability of a supramolecular framework by filling void space, which increases the density and the abundance of repulsive forces that prevent framework collapse. Increase the mechanical strength of the material, Is although they decrease the surface area and porosity of the structures as compared to their non-interpenetrated counterparts. Nevertheless, many interpenetrated MOFs exhibit excellent gas separation and selectivity characteristics due to their tunable

pore sizes. 16–18 In addition to the interpenetrated Zr-based 46 MOF investigated in this study, other interpenetrated Zr-based 47 MOFs have been reported. 19–22 Among these, the UiO-66 type 48 interpenetrated MOFs have been well known. 23–29 Other 49 systems that exhibit interpenetration were found during 50 isoreticular expansion of the linkers and have either ditopic 30–34 51 or tetratopic linkers, 35–38 which makes the relatively short 52 tritopic linker used in this study a unique case. Herein, we 53 explore the transient catenation processes between two different 54 interpenetrations of a 3,8-connected Zr-based MOF, known as 55 NU-1200 and STA-26 in its non-interpenetrated and interpenetrated forms, respectively.

Contemporary framework interpenetration studies rely 58 heavily on bulk characterization techniques. ¹⁸ However, 59 investigations into catenation processes via direct imaging at 60 the single-particle limit have not yet been performed. While 61 single-crystal X-ray diffraction (SCXRD) can be used to study 62

Received: October 28, 2020



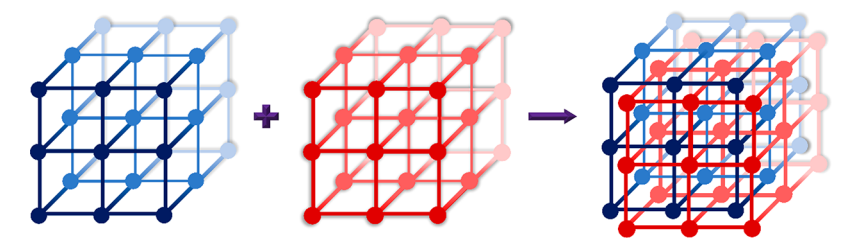


Figure 1. Schematic of non-interpenetrated frameworks and the doubly interpenetrated analogue.

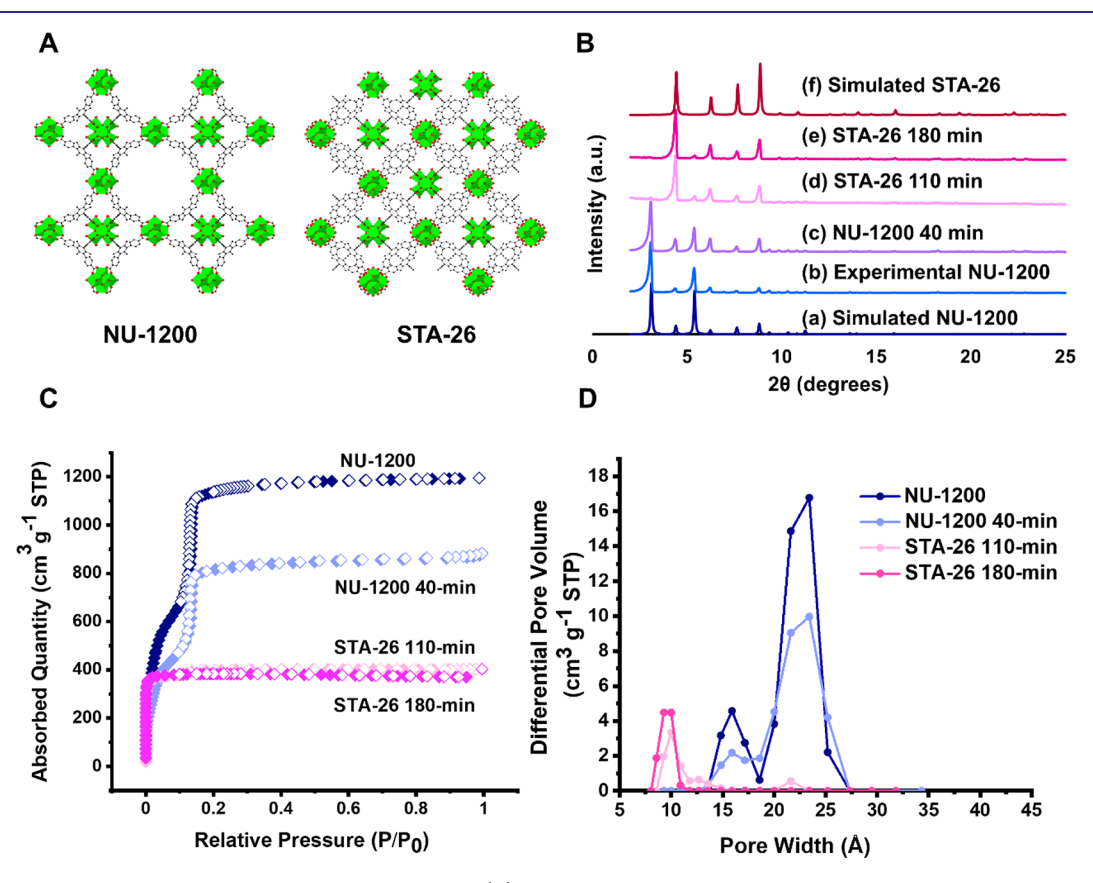


Figure 2. (A) NU-1200 and its interpenetrated analogue STA-26. (B) PXRD patterns of non-interpenetrated NU-1200 transiently transforming to interpenetrated STA-26 over variable reaction times. (C) Nitrogen sorption isotherms and (D) NLDFT-calculated pore size distributions of NU-1200 crystals transforming to STA-26 crystals over variable reaction times.

63 single particles, the indirectly obtained structure is extracted from the average positions of atoms in a crystal. This can become challenging to interpret when positional or substitutional disorder is present. Furthermore, single-crystal X-ray diffraction evaluates individual particles, which may not be representative of the bulk. In this work, we examine the zirconium cluster-based 69 non-interpenetrated NU-1200 MOF and the analogous doubly 70 interpenetrated STA-26 MOF at the single-particle level using 71 high-resolution transmission electron microscopy (TEM) coupled with an automated postprocessing script that analyzes 73 interpenetration across many images. These single-particle 74 studies are complemented by ensemble characterization 75 techniques such as powder X-ray diffraction (PXRD) and 76 adsorption isotherms with several probe molecules, including a 77 structural mimic for a chemical warfare agent. These 78 investigations reveal that catenation occurs in a near-stepwise 79 process within individual particles, which leads to mixtures of 80 pure phases of the interpenetrated and non-interpenetrated 81 structures rather than partially catenated particles. This

observation led us to study the thermodynamics and mechanical 82 properties of both pure phases via density functional theory 83 (DFT), in situ synchrotron X-ray diffraction, and nano-84 indentation experiments. Collectively, these studies enable the 85 reliable characterization of two different interpenetrated and 86 non-interpenetrated Zr-based MOFs and reveal their promise 87 for applications where demanding mechanical stresses are 88 encountered, including the storage of toxic chemical warfare 89 agents. ^{39,40}

■ RESULTS AND DISCUSSION

Herein, we characterize the properties of two distinct zirconium 92 cluster-based, 3,8-connected MOFs (Figure 2A). Each MOF 93 f2 features 4,4',4"-(2,4,6-trimethylbenzene-1,3,5-triyl)tribenzoic 94 acid (TMTB) linkers and $Zr_6(\mu_3\text{-OH})_4(\mu_3\text{-O})_4(OH)_4(OH_2)_4$ 95 Zr_6 -oxo cluster metal nodes. The tritopic TMTB linkers and 8-96 connected Zr_6 -oxo clusters assemble to form the non-inter-97 penetrated NU-1200, which possesses 14 Å diameter sodalite 98 cages and mesoporous 1D channels that are 20 Å in width. The 99

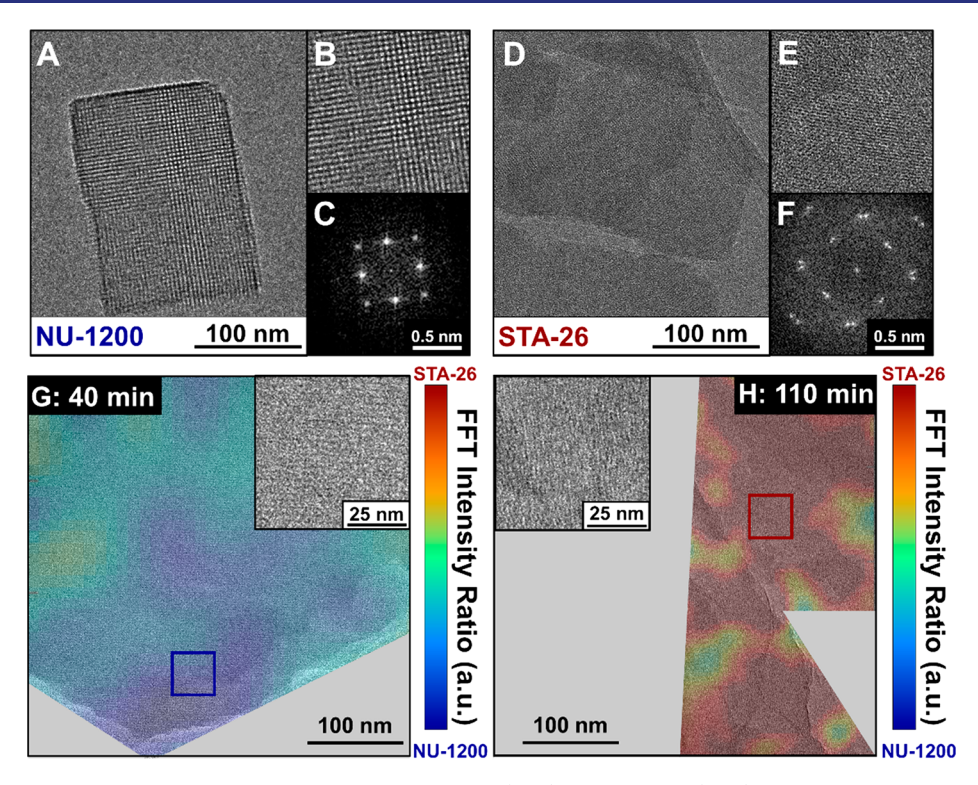


Figure 3. High-resolution transmission electron micrographs of pure-phase (A, B) NU-1200 and (D, E) STA-26. Fourier transforms of (C) NU-1200 and (F) STA-26. (G) Transmission electron micrograph obtained after 40 min of reaction revealing a predominant non-interpenetrated structure. Lattice-resolution image of the blue boxed region in G, showing a NU-1200 structure. (H) Transmission electron micrograph obtained after 110 min of reaction revealing a predominant interpenetrated structure. Lattice-resolution image of the red boxed region in G, showing an STA-26 structure. Gray regions indicate void space, lacey carbon substrate, or damaged crystallites.

100 NU-1200 MOF features the topology (cubic clusters and 101 triangular ligands) and crystallizes in the $Pm\overline{3}m$ space group. 41,42 102 Additional characterization data are available in the SI (Figures

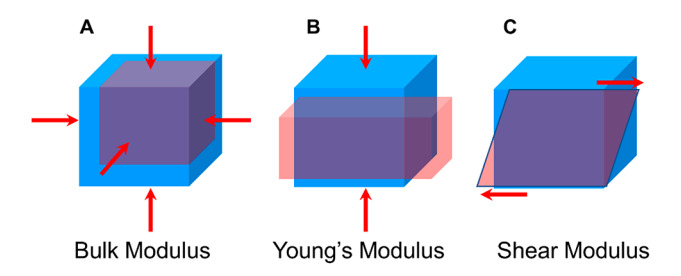
Wright, Prasad, and co-workers reported that the same TMTB 104 105 linker and Zr₆-oxo cluster metal node produces STA-26, a 106 doubly interpenetrated analogue of NU-1200.43 The authors 107 synthetically targeted the structure by changing the identity and concentration of the modulating species present during the synthesis. The STA-26 MOF possesses the same topology but is 110 microporous rather than mesoporous as a result of the second lattice being displaced by $\left[\frac{1}{2},\frac{1}{2},\frac{1}{2}\right]$ from the original non-

112 interpenetrated NU-1200 framework. This displacement 113 means that the vertex of one sublattice is in the exact center of 114 the sodalite cages of the other, while the diameter of the octahedral cages remains the same (14 Å). The STA-26 MOF 116 exhibits Im3m symmetry.

However, we observed that the interpenetration can be 118 initiated postsynthetically, and the degree of interpenetration 119 between these two networks could be controlled by regulating the reaction time. We initiated the interpenetration of NU-1200 to STA-26 by exposing 20 mg of thermally activated NU-1200 to solution of DMF/HCOOH that is 2.5:1 by volume at 120 °C for 40, 110, or 180 min and referred to as NU-1200-x or STA-26-124 x where x indicates the time that MOF particles spend in the 125 DMF/HCOOH solution. We found that this transient 126 catenation process was complete after 110 min. We monitored 127 this transition using PXRD (Cu K α 1 radiation, λ = 1.540 56 Å) 128 by tracking the disappearance of the peak at $2\theta = 3.1^{\circ}$, which 129 corresponds to the NU-1200 (100) Bragg feature, and the 130 growth of the 4.42° feature, which corresponds to the (110)

reflection of STA-26 (Figure 2B). We posit a mechanism for this 131 process, but it is preliminary, as we do not have comprehensive 132 experimental data to explain the process.⁴⁴ Nitrogen isotherms 133 obtained along the course of this transition demonstrated a 134 decrease in gravimetric adsorption capacity consistent with the 135 interpenetrated framework decreasing the total void space of the 136 MOF. Similarly, the extracted pore sizes calculated from the 137 nonlocal density functional theory (NLDFT) model for pillared 138 clay reveal that during this transition the mesopore of NU-1200 139 (20 Å) disappears, and after 110 min of soaking in formic acid/ 140 DMF solution, only the STA-26 micropore (10 Å) is observed. 141 To determine if the phase transition to the denser STA-26 142 interpenetrated phase could be reversed to the mesoporous NU- 143 1200, which could imply entropic control between the two, we 144 applied the original synthesis conditions to activated STA-26. 145 However, we found that we could not reverse the inter- 146 penetration trend we observe (Figure S4).

TEM Imaging and Automated Interpenetration Map- 148 ping. Despite the numerous investigations into framework 149 catenation processes, 18 there still exists a limited understanding 150 of how this process occurs within single particles. Recently, highresolution transmission electron microscopy (HR-TEM) 152 hardware and imaging techniques have been developed to 153 study beam-sensitive materials, such as MOFs. 45 Here, we 154 combine those advances with an automated postprocessing 155 Fourier transform mapping technique to explore the transition 156 of NU-1200 to STA-26 at the single-particle limit (Figure 3). We 157 f3 first imaged samples of the non-interpenetrated NU-1200 and 158 interpenetrated STA-26. Fast Fourier transforms (FFTs) of 159 MOF particles on the [100] zone axis showed the expected 160 lattice symmetries of Pm3m and Im3m for NU-1200 and STA- 161



MOF	Bulk modulus (K)	Young's modulus (E)	Shear modulus (G)
NU-1200	8.1 GPa	2.3 GPa	0.8 GPa
STA-26	15.1 GPa	3.8 GPa	1.3 GPa

Figure 4. Illustrations of elastic properties studied in this article. (A) Bulk modulus (K): measure of elastic resistance to hydrostatic compression. (B) Young's modulus (E): measure of resistance in length during uniaxial tension or compression. (C) Shear modulus (G): measure of the resistance when subjected to opposing shear forces. Computational mechanical properties of non-interpenetrated NU-1200 and interpenetrated STA-26.

162 26, respectively (Figure S5). Due to this difference in symmetry 163 and accompanying difference in electron density contrast, these 164 two lattices can be resolved by evaluating the relative intensity 165 ratios of the FFT features at 0.36 and 0.49 nm⁻¹ that correspond 166 to real spacings of 2.8 and 2.0 nm, respectively. Using this 167 understanding, we developed a postprocessing script, which 168 automatically rasters a small region-of-interest across an image, 169 extracts the Fourier transform of that subimage, and then assigns 170 the dominant interpenetration within that region based on the 171 relative intensity ratios of the FFT features mentioned above 172 (Figure S6). This method allows us to spatially resolve the 173 interpenetration of entire crystallites across a series of images. 174 When this method was applied to pure crystal phases, we found 175 that the script could reliably disambiguate the two phases 176 (Figures S7 and S8).

177 We then applied the same technique to microtome-cut 178 intermediate time point samples, NU-1200 40 min and STA-26 179 110 min, which we obtained along the course of the 180 interpenetration transition. This approach allows us to statisti-181 cally investigate the process of transient catenation. In particular, 182 we investigated whether interpenetration occurs gradually 183 across all crystals within a sample or whether two predominantly 184 pure phases are present at all times, which would be challenging 185 to resolve using bulk techniques such as powder X-ray 186 diffraction or nitrogen adsorption at 77 K.

From our postimaging analysis, we predominantly observed 187 188 that pure phases were present at all times, which suggests that once an interpenetration transition is initialized, it occurs rapidly 190 and completely. Across several images of NU-1200 40 min (Figures S9 and S10), we found that nearly all particles were 192 obtained as pure non-interpenetrated NU-1200 (Figure S13). However, a select number of particles were obtained as the pure STA-26 phase. In contrast, we found the images of the STA-26 195 110 min sample (Figures S11 and S12) dominated by the 196 interpenetrated STA-26 crystallites (Figure S14). In rare 197 instances, we observed minor, residual NU-1200 non-interpenetrated domains at the fringes of these crystallites (Figures 199 S15-S18), which may account for the minor X-ray diffraction 200 features observed at prolonged reaction times. The noninterpenetrated lattice being confined at the edge of these 202 intermixed particles indicates that edges are the final location to 203 interpenetrate. Taken together, these results suggest that 204 catenation occurs rapidly from NU-1200 to STA-26 within 205 single particles. This contrasts with the possibility that the 206 catenation process occurs gradually across all crystallites, which 207 would lead to the prevalent observation of intermixed phases

within single particles. This finding has implications for the 208 physical properties of samples undergoing catenation, which in 209 this case are likely to behave similarly to physical mixtures of 210 pure phases. More investigation is needed to resolve the 211 thermodynamic and kinetic underpinnings of this transition.

Physical Mixtures of Multiple Phases. From our findings 213 that intermediate samples were predominantly single-phase 214 particles, we decided to compare our ensemble measurements 215 performed on intermediate samples with those of physical 216 mixtures of pure NU-1200 and pure STA-26 phases. We 217 observed the same decrease in nitrogen sorption capacity, 218 reduction in the differential pore volume and pore size, and 219 change in PXRD pattern for the physical mixtures (Figure S19) 220 as MOF samples measured during the interpenetration process 221 (Figure 2).

Our ensemble and direct imaging findings lead us to conclude 223 that the interpenetration of NU-1200 occurs very quickly, with 224 some percentage of crystals in intermediate samples being 225 doubly interpenetrated STA-26 or non-interpenetrated NU- 226 1200. This contrasts with our initial hypothesis that we 227 synthesized MOFs exhibiting partial interpenetration. Com- 228 bined with our TEM mapping results, we conclude that the 229 decrease in adsorbed nitrogen and concurrent decrease in pore 230 volume dominantly arise from different ratios of the two phases. 231 The total uptake of N_2 from the nitrogen sorption isotherms of 232 the physical mixtures (Figure S19) displays a linear relationship 233 $(R^2 = 0.96)$ from non-interpenetrated to doubly interpenetrated 234 (Figure S20). Additionally, we observed a linear relationship (R^2 235 = 0.96) between the total pore volume (cm 3 g $^{-1}$) plotted and the 236 ratio of pure crystals that are mixed (Figure S21). These 237 observations are largely consistent with our observation of a 238 stepwise transition from the NU-1200 to the STA-26 phase, 239 rather than gradual framework interpenetration within single 240 particles.

Reinforced Mechanical Strength of Interpenetrated 242 Lattices. Previous work in the MOF field has established 243 interesting pressure-induced behavior in framework materials, 244 including the discovery of new phases, polymorphism, negative 245 linear compressibility, and single crystal to single crystal phase 246 transitions, among others. 46–50 While it is generally understood 247 that physical properties of MOFs are affected by inter-248 penetration, very few studies have explored the differences 249 between mechanical strength of differentially interpenetrated 250 chemically identical networks. To our knowledge this is the 251 first study to combine DFT computations and experimental 252 work to determine the effect of interpenetration on the 253

254 hydrostatic, uniaxial, and shear stress on a MOF structure. 255 Studying the bulk mechanical properties of differently inter-256 penetrated structures⁵¹ is crucial for the use of MOFs in 257 commercial applications which require that powdered MOF 258 samples be processed into shaped constructs such as pellets, 259 extrudates, or composite materials.^{52–54}

We investigated NU-1200 and STA-26 using DFT to obtain values for the bulk modulus (*K*), the Young's modulus (*E*), and the shear modulus (*G*) (Figure 4). Each structural model behaved well under energy minimization, with lattice parameters in good agreement with the experimentally obtained crystal structures. The interpenetrated STA-26 structure is 223 kJ mol⁻¹ more stable than the non-interpenetrated NU-1200 framework. This value agrees with other large-pore interese penetrated frameworks and reveals that the non-interpenetrated phase is metastable compared to its denser interpenetrated analogue (see Supporting Information for additional computational details). This finding is in line with other additional classes of porous materials (mesoporous silicas and siliceous zeolites) solves along with other MOF frame-

The bulk modulus (K) of a material is a measure of the elastic 276 resistance to hydrostatic compression and related to the ratio of 277 volumetric stress over the volumetric strain (K = -V dP/dV) in an isothermal process. The Young's modulus (E) is a measure of 279 a material's ability to deform under uniaxial constraint (tension or compression). The Young's modulus is equivalent to the tensile stress over the tensile strain $(E = \sigma/\epsilon)$. The shear 282 modulus ($G = Fl/A\Delta x$) is the measure of deformation of one 283 surface of a material while an opposite face of the material 284 experiences an opposing force. The shear modulus is the ratio of 285 shear stress to shear strain. Our DFT results show that 286 interpenetration nearly doubles the value of the bulk modulus 287 and increases the Young's and shear moduli by 60%. These 288 calculations reveal that the interpenetrated STA-26 framework is 289 stiffer and more mechanically robust than the NU-1200 non-290 interpenetrated structure.

Table 1. Experimental Properties of Non-interpenetrated NU-1200 and Interpenetrated STA-26

MOF	experimental bulk modulus (K)	experimental Young's modulus (E)
NU-1200	$5.7 \pm 0.3 \text{ GPa}$	2.3 GPa
STA-26	$21.1 \pm 0.5 \text{ GPa}$	3.8 GPa

We determined the bulk modulus (K) for the NU-1200 and 292 STA-26 MOFs using in situ synchrotron PXRD using a diamond 293 anvil cell (DAC) pressure apparatus at the 17-BM beamline (λ = 0.45418 Å) at the Advanced Photon Source at Argonne 295 National Laboratory. The PXRD peaks of the two MOFs shift to 296 higher angles of diffraction upon the application of modest 297 pressures, which we applied up to 0.55 GPa (Figures S28 and \$29) and indicate compression along all crystallographic axes of 299 the MOF sample. By first extracting the unit cell volume from the location of our diffraction features and then using a secondorder Birch-Murnaghan equation of state, we determine the 302 bulk modulus of each MOF (Figure 5A). The plots of the unit 303 cell volumes vs pressure reveal the interpenetrated STA-26 304 MOF has a higher bulk modulus ($K = 21.1 \pm 0.5$ GPa) than the 305 non-interpenetrated NU-1200 ($K = 5.7 \pm 0.3$ GPa) (Figure 306 S27). The experimental data for the interpenetrated STA-26 307 MOF align well with the second-order model, even though the

computationally derived value for the bulk modulus of the 308 interpenetrated MOF is 6.0 GPa lower than the experimental 309 value. The difference between the values for the bulk modulus of 310 NU-1200 is only 2.4 GPa. However, the experimental data 311 exhibit deviations from the best fit using a second-order Birch—312 Murnaghan equation of state (Figure S27). This discontinuity at 313 low pressures may indicate mechanically induced phase 314 transitions. 60,61

pubs.acs.org/JACS

Indeed, the computationally derived elastic tensors support 316 that phase transitions may occur at low pressures in NU-1200. 317 We found that the tetragonal shear modulus, $C_{11}-C_{12}$, value of 318 NU-1200 is the lowest eigenvalue of all calculated elastic tensors 319 for both structures, which suggests that this system is the least 320 robust to elastic mechanical deformation and is therefore prone 321 to phase transitions. In particular, $C_{11}-C_{12}$ is 0.6 GPa for the 322 non-interpenetrated NU-1200 phase, meaning the system will 323 likely undergo a phase transition upon the application of modest 324 amounts of pressure (Figure S25). Due to the large coordination 325 number of NU-1200, it remains mechanically stable at ambient 326 pressure, while other highly porous MOFs with low shear 327 moduli have been shown to be unstable under guest removal. 62 328 Therefore, the tetragonal shear is the softest mode of 329 deformation.

In addition to the bulk modulus, we also determined the 331 Young's moduli (E) using single-crystal nanoindentation 332 methods (Figure 5B). We plotted the load-displacement data 333 (Figures S30 and S31) from each indentation and obtained the 334 Young's modulus and hardness as a function of indentation 335 depth using the method proposed by Oliver and Pharr. 63 By 336 averaging measurements over five indentations, we assign the 337 Young's modulus of NU-1200 as 2.9 GPa with a hardness of 100 338 MPa and the Young's modulus of STA-26 as 4.6 GPa with a 339 hardness of 300 MPa. These values agree well with those 340 determined using computational methods, which also reveal that 341 the non-interpenetrated NU-1200 is softer than the STA-26 342 under uniaxial compression. Collectively, our experimental and 343 computational findings reveal that STA-26 is considerably more 344 structurally robust than NU-1200. These findings demonstrate 345 that interpenetrated MOFs are likely more stable to all forms of 346 mechanical stress, including those listed here (hydrostatic, 347 uniaxial, and shear) than their non-interpenetrated, chemically 348 identical analogues. This indicates that if a sample includes a 349 mixture of interpenetrated and non-interpenetrated crystals, 350 processing conditions are limited by the less stable MOF. 351 Moreover, this observation suggests that if you have mixed 352 phases, they are more likely to deform under mechanical stress. 353

Complementary Gas Sorption of Physically Mixed 354 MOF Systems. One potential application for MOFs is the 355 capture and detoxification of chemical warfare agents such as a 356 potent blistering agent, mustard gas. 64,65 Since the inter- 357 penetrated STA-26 and non-interpenetrated NU-1200 MOFs 358 exhibit different pore structures and N2 uptake capacities, we 359 hypothesized that they would likely exhibit different adsorption 360 characteristics for *n*-hexane, which we used as a structural mimic 361 for mustard gas due to similarity in size and hydrophobicity of 362 these two molecules.⁶⁶ The uptake trends we report can only be 363 directly applied to *n*-hexane; however, we can use this 364 hydrocarbon as a model to begin to understand more complex 365 compounds, such as mustard gas. We collected n-hexane 366 adsorption isotherms in both pure-phase MOFs and variable 367 mixtures of the two pure phases. We observed a much greater 368 uptake of n-hexane at lower partial pressure in the inter- 369 penetrated microporous STA-26 MOF than in the mesoporous 370

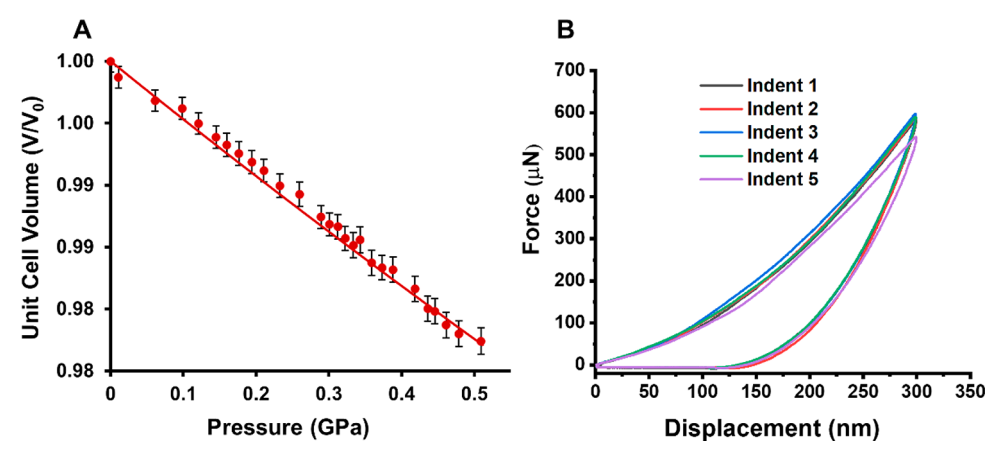


Figure 5. (A) Relative lattice compression of interpenetrated STA-26 obtained using *in situ* synchrotron PXRD to determine the bulk modulus. Line represents the second-order Birch—Murnaghan equation-of-state fit to the data. (B) Example of force vs displacement curves of an interpenetrated STA-26 sample obtained using single-crystal nanoindentation to determine the Young's modulus.

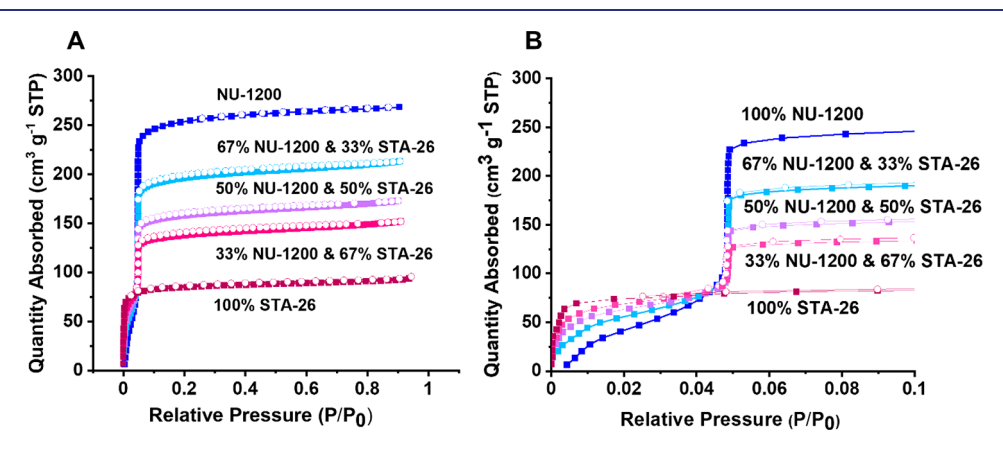


Figure 6. (A) n-Hexane adsorption isotherms for a physical mixture of pure-phase samples. (B) Blow up of the $0-0.1 \ P/P_0$ region for n-hexane adsorption isotherms for a physical mixture of pure-phase samples.

371 non-interpenetrated NU-1200 MOF. The 100% STA-26 sample 372 reaches saturation at 0.01 P/P_0 , while the 100% NU-1200 373 sample reaches saturation at 0.05 P/P_0 (Figure 6). This suggests 374 that the interpenetrated MOF will exhibit better performance 375 for low-concentration capture of mustard gas, but the non-376 interpenetrated NU-1200 will have an overall higher capacity for 377 toxic gas capture. To support this observation, we plotted the 378 total uptake of hexanes (cm³ g⁻¹) plotted against each sample 379 (Figure S23) and found a linear relationship ($R^2 = 0.98$) 380 between the two. This indicates that benefits may exist by 381 combining different interpenetrations of MOF crystallites 382 within a single capture device.

383 CONCLUSIONS

384 In summary, we have investigated the interpenetration of the 385 zirconium cluster-based mesoporous NU-1200 MOF to the 386 chemically identical microporous STA-26 MOF at the bulk and 387 single-particle limits. Using bulk methods, one may propose that 388 we have obtained partially interpenetrated crystallites. However, 389 we find that our X-ray diffraction, gas adsorption, and 390 transmission electron microscopy measurements better describe 391 our system as statistical mixtures of crystallites with integral 392 values of interpenetration, rather than fractionally occupied 393 phases. This suggests that interpenetration, once initialized, 394 occurs rapidly. Experimental and computational evaluation of 395 the mechanical properties for each framework revealed that the

interpenetrated phase is more mechanically robust and 396 thermodynamically stable than its non-interpenetrated counter-397 part. Finally, we find that these two phases exhibit radically 398 different uptake behavior for *n*-hexane. Isotherms of mixed-399 phase systems show intermediate uptake behavior, which 400 suggests that an opportunity exists to systematically tune 401 adsorption characteristics by mixtures of variably interpene-402 trated crystallites, which we have shown can be obtained by *de* 403 *novo* synthetic methods. Future studies should aim to explore 404 mechanistic processes and physical characteristics related to 405 interpenetrated MOFs more broadly, which we suspect will be 406 an important area of study for the commercial deployment of 407 these materials.

ASSOCIATED CONTENT

Supporting Information

The Supporting Information is available free of charge at 411 https://pubs.acs.org/doi/10.1021/jacs.0c11266.

Physical methods and instrumentation, syntheses of 413 TMTB linker and Zr-MOFs, PXRD data, NMR data, 414 SEM and TEM images, mapping script, computational 415 methods, and mechanical properties measurements 416 (PDF)

409

410

488

489

18	AU	IHOR	INFO)KM#	ADIT <i>P</i>

19	Corres	ponding	Authors
----	--------	---------	---------

4

Nathan C. Gianneschi – Department of Chemistry, 420 International Institute of Nanotechnology, Department of 421 Chemistry, and Department of Biomedical Engineering, 422 Department of Materials Science & Engineering, Department 423 of Pharmacology, Simpson-Querrey Institute, Chemistry of Life 424 Processes Institute, Lurie Cancer Center, Northwestern 425 University, Evanston, Illinois 60208, United States; 426 orcid.org/0000-0001-9945-5475; 427 Email: nathan.gianneschi@northwestern.edu 42.8 Omar K. Farha – Department of Chemistry, International 429 Institute of Nanotechnology, Department of Chemistry, and 430 Department of Chemical and Biological Engineering, 431 Northwestern University, Evanston, Illinois 60208, United 432 States; o orcid.org/0000-0002-9904-9845; Email: o-433 farha@northwestern.edu 434

435 Authors

436

437

438

439

440

441

442

443

444

445

446 447

448

449

450

451

452

453

454

455

456

457

458

459

460

461

462 463

464

465

466

467

468

470

471

472

473

474

475

476

477

478 479

Lee Robison — Department of Chemistry and International Institute of Nanotechnology, Department of Chemistry, Northwestern University, Evanston, Illinois 60208, United States; orcid.org/0000-0002-7419-4499

Xinyi Gong — Department of Chemistry and International Institute of Nanotechnology, Department of Chemistry, Northwestern University, Evanston, Illinois 60208, United States; orcid.org/0000-0003-0295-3959

Austin M. Evans – Department of Chemistry, Northwestern University, Evanston, Illinois 60208, United States;

orcid.org/0000-0002-3597-2454

Florencia A. Son — Department of Chemistry, Northwestern University, Evanston, Illinois 60208, United States;
orcid.org/0000-0002-7524-3774

Xingjie Wang — Department of Chemistry, Northwestern University, Evanston, Illinois 60208, United States; orcid.org/0000-0002-5802-9944

Louis R. Redfern — Department of Chemistry, Northwestern University, Evanston, Illinois 60208, United States;
occid.org/0000-0002-0209-064X

Megan C. Wasson — Department of Chemistry, Northwestern University, Evanston, Illinois 60208, United States; orcid.org/0000-0002-9384-2033

Zoha H. Syed — Department of Chemistry, Northwestern University, Evanston, Illinois 60208, United States; Chemical Sciences and Engineering Division, Argonne National Laboratory, Lemont, Illinois 60439, United States; orcid.org/0000-0002-0074-2253

Zhijie Chen — Department of Chemistry, Northwestern University, Evanston, Illinois 60208, United States; orcid.org/0000-0001-9232-7382

Karam B. Idrees — Department of Chemistry, Northwestern University, Evanston, Illinois 60208, United States; orcid.org/0000-0002-9603-3952

Timur Islamoglu — International Institute of Nanotechnology, Department of Chemistry, Northwestern University, Evanston, Illinois 60208, United States; orcid.org/0000-0003-3688-9158

Massimiliano Delferro − Chemical Sciences and Engineering Division, Argonne National Laboratory, Lemont, Illinois 60439, United States; orcid.org/0000-0002-4443-165X

William R. Dichtel — Department of Chemistry, Northwestern University, Evanston, Illinois 60208, United States;
o orcid.org/0000-0002-3635-6119

François-Xavier Coudert — Chimie ParisTech, PSL University, 480
CNRS, Institut de Recherche de Chimie Paris, 75005 Paris, 481
France; orcid.org/0000-0001-5318-3910
Complete contact information is available at: 483
https://pubs.acs.org/10.1021/jacs.0c11266

Author Contributions
#L.R. and X.G. contributed equally.

Notes
486

The authors declare no competing financial interest.

ACKNOWLEDGMENTS

O.K.F. gratefully acknowledges the financial support from the 490 Air Force Research Laboratory (FA8650-15-2-5518) for the 491 MOF materials synthesis. O.K.F. gratefully acknowledges 492 support from the Defense Threat Reduction Agency 493 (HDTRA1-19-1-0007) for the physical stability and sorption 494 measurements. O.K.F. and N.C.G. gratefully acknowledge 495 support from National Science Foundation's MRSEC program 496 (grant number NSF DMR-1720139). N.C.G. acknowledges the 497 Army Research Office for support of the development of TEM 498 for MOFs (W911NF-15-1-0189). M.D. acknowledges the 499 financial support from the Inorganometallic Catalyst Design 500 Center, an Energy Frontier Research Center funded by the U.S. 501 Department of Energy, Office of Science, Basic Energy Sciences, 502 under award no. DE-SC0012702. F.-X.C. is supported by the 503 Agence Nationale de la Recherche (project MATAREB, ANR- 504 18-CE29-0009-01), and access to HPC platforms was provided 505 by a GENCI grant (A0090807069). X.G. gratefully acknowl- 506 edges the support of the Northwestern University Ryan 507 Fellowship granted by the International Institute of Nano- 508 technology and The Graduate School at Northwestern 509 University. M.C.W. and Z.H.S. are supported by the NSF 510 Graduate Research Fellowship under grant DGE-1842165. 511 A.M.E. is supported by the NSF Graduate Research Fellowship 512 under grant DGE-1324585. F.A.S. is supported by the 513 Department of Defense (DoD) through the National Defense 514 Science & Engineering Graduate (NDSEG) Fellowship 515 Program. The authors thank Dr. Yuyang Wu and Dr. Yongbo 516 Zhang for assistance in acquiring and interpreting the solid state 517 NMR data reported herein. Use was made of the IMSERC X-ray 518 facility at Northwestern University, which has received support 519 from the Soft and Hybrid Nanotechnology Experimental 520 (SHyNE) Resource (NSF ECCS-1542205), the State of Illinois, 521 and the International Institute for Nanotechnology (IIN). Use 522 was made of NMR-Hg400-solids at Northwestern University, 523 which has received support from National Science Foundation 524 (CHE-9871268) and International Institute for Nanotechnol- 525 ogy (IIN). This work made use of the SPID facility of 526 Northwestern University's NUANCE Center, which has 527 received support from the Soft and Hybrid Nanotechnology 528 Experimental (SHyNE) Resource (NSF ECCS-1542205); the 529 MRSEC program (NSF DMR-1720139) at the Materials 530 Research Center; the International Institute for Nanotechnol- 531 ogy (IIN); the Keck Foundation; and the State of Illinois, 532 though the IIN. This work made use of the EPIC facility of 533 Northwestern University's NUANCE Center, which has 534 received support from the SHyNE Resource (NSF ECCS- 535 1542205), the MRSEC program (NSF DMR-1720139) at the 536 Materials Research Center, the IIN, the Keck Foundation, and 537 the State of Illinois through the IIN. This research used 538 resources of the Advanced Photon Source, a U.S. Department of 539

540 Energy (DOE) Office of Science User Facility operated for the 541 DOE Office of Science by Argonne National Laboratory under 542 contract no. DE-AC02-06CH11357.

REFERENCES

- 544 (1) Zhou, H. C.; Long, J. R.; Yaghi, O. M. Introduction to Metal—545 Organic Frameworks. *Chem. Rev.* **2012**, *112* (2), *673*–*674*.
- 546 (2) Perry, J. J., IV; Perman, J. A.; Zaworotko, M. J. Design and 547 synthesis of metal—organic frameworks using metal—organic polyhedra 548 as supermolecular building blocks. *Chem. Soc. Rev.* **2009**, 38 (5), 1400—549 1417.
- 550 (3) Howarth, A. J.; Liu, Y.; Li, P.; Li, Z.; Wang, T. C.; Hupp, J. T.; 551 Farha, O. K. Chemical, Thermal and Mechanical Stabilities of Metal—552 Organic Frameworks. *Nat. Rev. Mater.* **2016**, *1* (3), 15018.
- 553 (4) Yuan, S.; Qin, J.-S.; Lollar, C. T.; Zhou, H.-C. Stable Metal—554 Organic Frameworks with Group 4 Metals: Current Status and Trends. 555 ACS Cent. Sci. 2018, 4 (4), 440–450.
- 556 (5) Bon, V.; Senkovska, I.; Weiss, M. S.; Kaskel, S. Tailoring of 557 network dimensionality and porosity adjustment in Zr- and Hf-based 558 MOFs. *CrystEngComm* **2013**, *15* (45), 9572–9577.
- 659 (6) Jiang, H.; Zhang, W.; Kang, X.; Cao, Z.; Chen, X.; Liu, Y.; Cui, Y. Topology-Based Functionalization of Robust Chiral Zr-Based Metal—S61 Organic Frameworks for Catalytic Enantioselective Hydrogenation. *J. S62 Am. Chem. Soc.* **2020**, *142* (21), 9642–9652.
- 563 (7) Wasson, M. C.; Buru, C. T.; Chen, Z.; Islamoglu, T.; Farha, O. K. 564 Metal—Organic Frameworks: A Tunable Platform to Access Single-Site 565 Heterogeneous Catalysts. *Appl. Catal., A* **2019**, 586, 117214.
- 566 (8) Wang, S.; Lee, J. S.; Wahiduzzaman, M.; Park, J.; Muschi, M.; 567 Martineau-Corcos, C.; Tissot, A.; Cho, K. H.; Marrot, J.; Shepard, W.; 568 Maurin, G.; Chang, J.-S.; Serre, C. A Robust Large-Pore Zirconium 569 Carboxylate Metal—Organic Framework for Energy-Efficient Water-570 Sorption-Driven Refrigeration. *Nat. Energy* **2018**, 3 (11), 985—993.
- 571 (9) Chen, Z.; Li, P.; Zhang, X.; Li, P.; Wasson, M. C.; Islamoglu, T.; 572 Stoddart, J. F.; Farha, O. K. Reticular Access to Highly Porous acs-573 MOFs with Rigid Trigonal Prismatic Linkers for Water Sorption. *J. Am.* 574 *Chem. Soc.* **2019**, *141* (7), 2900–2905.
- 575 (10) Xu, W.; Yaghi, O. M. Metal–Organic Frameworks for Water 576 Harvesting from Air, Anywhere, Anytime. ACS Cent. Sci. 2020, 6 (8), 577 1348–1354.
- 578 (11) Chen, Z.; Hanna, S. L.; Redfern, L. R.; Alezi, D.; Islamoglu, T.; 579 Farha, O. K. Reticular chemistry in the rational synthesis of functional s80 zirconium cluster-based MOFs. *Coord. Chem. Rev.* **2019**, 386, 32–49.
- 581 (12) Lin, R.-B.; Xiang, S.; Xing, H.; Zhou, W.; Chen, B. Exploration of 582 porous metal—organic frameworks for gas separation and purification. 583 *Coord. Chem. Rev.* **2019**, 378, 87–103.
- 584 (13) Batten, S. R.; Robson, R. Interpenetrating Nets: Ordered, 585 Periodic Entanglement. *Angew. Chem., Int. Ed.* **1998**, 37 (11), 1460–586 1494.
- 587 (14) Chen, B.; Eddaoudi, M.; Hyde, S. T.; O'Keeffe, M.; Yaghi, O. M. 588 Interwoven Metal-Organic Framework on a Periodic Minimal Surface 589 with Extra-Large Pores. *Science* **2001**, *291* (5506), 1021–1023.
- 590 (15) Ferguson, A.; Liu, L.; Tapperwijn, S. J.; Perl, D.; Coudert, F.-X.; 591 Van Cleuvenbergen, S.; Verbiest, T.; van der Veen, M. A.; Telfer, S. G. 592 Controlled Partial Interpenetration in Metal—Organic Frameworks. 593 *Nat. Chem.* **2016**, 8 (3), 250–257.
- 594 (16) Fernandez, C. A.; Liu, J.; Thallapally, P. K.; Strachan, D. M. 595 Switching Kr/Xe Selectivity with Temperature in a Metal—Organic 596 Framework. *J. Am. Chem. Soc.* **2012**, 134 (22), 9046—9049.
- 597 (17) Liang, W.; Bhatt, P. M.; Shkurenko, A.; Adil, K.; Mouchaham, G.; 598 Aggarwal, H.; Mallick, A.; Jamal, A.; Belmabkhout, Y.; Eddaoudi, M. A 599 Tailor-Made Interpenetrated MOF with Exceptional Carbon-Capture 600 Performance from Flue Gas. *Chem.* **2019**, *5* (4), 950–963.
- 601 (18) Jiang, H.-L.; Makal, T. A.; Zhou, H.-C. Interpenetration Control 602 in Metal—Organic Frameworks for Functional Applications. *Coord.* 603 *Chem. Rev.* **2013**, 257 (15), 2232–2249.
- 604 (19) Zhang, Y.; Zhang, X.; Chen, Z.; Otake, K.-i.; Peterson, G. W.; 605 Chen, Y.; Wang, X.; Redfern, L. R.; Goswami, S.; Li, P.; Islamoglu, T.; 606 Wang, B.; Farha, O. K. A Flexible Interpenetrated Zirconium-Based

- Metal-Organic Framework with High Affinity toward Ammonia. 607 ChemSusChem 2020, 13 (7), 1710-1714. 608
- (20) Xu, X.; Li, S.; Liu, Q.; Liu, Z.; Yan, W.; Zhao, L.; Zhang, W.; 609 Zhang, L.; Deng, F.; Cong, H.; Deng, H. Isolated π -Interaction Sites in 610 Mesoporous MOF Backbone for Repetitive and Reversible Dynamics 611 in Water. ACS Appl. Mater. Interfaces 2019, 11 (1), 973–981.
- (21) Duan, Z.; Li, Y.; Xiao, X.; Huang, X.; Li, X.; Li, Y.; Zhang, C.; 613 Zhang, H.; Li, L.; Lin, Z.; Zhao, Y.; Huang, W. Interpenetrated Metal—614 Organic Frameworks with ftw Topology and Versatile Functions. ACS 615 Appl. Mater. Interfaces 2020, 12 (16), 18715—18722.
- (22) Kong, X.-J.; He, T.; Zhang, Y.-Z.; Wu, X.-Q.; Wang, S.-N.; Xu, 617 M.-M.; Si, G.-R.; Li, J.-R. Constructing new metal—organic frameworks 618 with complicated ligands from "One-Pot" in situ reactions. *Chem. Sci.* 619 **2019**, 10 (14), 3949–3955.
- (23) Chen, D.; Xing, H.; Wang, C.; Su, Z. Highly efficient visible-light- 621 driven CO2 reduction to formate by a new anthracene-based zirconium 622 MOF via dual catalytic routes. *J. Mater. Chem. A* **2016**, 4 (7), 2657– 623 2662.
- (24) Lippke, J.; Brosent, B.; von Zons, T.; Virmani, E.; Lilienthal, S.; 625 Preuße, T.; Hülsmann, M.; Schneider, A. M.; Wuttke, S.; Behrens, P.; 626 Godt, A. Expanding the Group of Porous Interpenetrated Zr-Organic 627 Frameworks (PIZOFs) with Linkers of Different Lengths. *Inorg. Chem.* 628 2017, 56 (2), 748–761.
- (25) Schaate, A.; Roy, P.; Preuße, T.; Lohmeier, S. J.; Godt, A.; 630 Behrens, P. Porous Interpenetrated Zirconium—Organic Frameworks 631 (PIZOFs): A Chemically Versatile Family of Metal—Organic Frame- 632 works. *Chem. Eur. J.* **2011**, *17* (34), 9320—9325.
- (26) Cavka, J. H.; Jakobsen, S.; Olsbye, U.; Guillou, N.; Lamberti, C.; 634 Bordiga, S.; Lillerud, K. P. A New Zirconium Inorganic Building Brick 635 Forming Metal Organic Frameworks with Exceptional Stability. *J. Am.* 636 Chem. Soc. **2008**, 130 (42), 13850–13851.
- (27) Marshall, R. J.; Griffin, S. L.; Wilson, C.; Forgan, R. S. 638 Stereoselective Halogenation of Integral Unsaturated C-C Bonds in 639 Chemically and Mechanically Robust Zr and Hf MOFs. *Chem. Eur. J.* 640 **2016**, 22 (14), 4870–4877.
- (28) Doan, T. L. H.; Nguyen, H. L.; Pham, H. Q.; Pham-Tran, N.-N.; 642 Le, T. N.; Cordova, K. E. Tailoring the Optical Absorption of Water- 643 Stable ZrIV- and HfIV-Based Metal—Organic Framework Photo- 644 catalysts. *Chem. Asian J.* **2015**, *10* (12), 2660—2668.
- (29) Zhang, D.; Yin, Q.; Li, L.; Liu, T.-F.; Chen, Y.-P. Two 646 interpenetrated metal-organic frameworks: The CH4 and CO2 647 adsorption and in-situ XRD studies. *Inorg. Chem. Commun.* **2019**, 648 108, 107503.
- (30) Marshall, R. J.; Kalinovskyy, Y.; Griffin, S. L.; Wilson, C.; Blight, 650 B. A.; Forgan, R. S. Functional Versatility of a Series of Zr Metal—651 Organic Frameworks Probed by Solid-State Photoluminescence 652 Spectroscopy. J. Am. Chem. Soc. 2017, 139 (17), 6253–6260.
- (31) Wang, H.; Yu, L.; Lin, Y.; Peng, J.; Teat, S. J.; Williams, L. J.; Li, J. 654 Adsorption of Fluorocarbons and Chlorocarbons by Highly Porous and 655 Robust Fluorinated Zirconium Metal—Organic Frameworks. *Inorg.* 656 *Chem.* **2020**, 59 (7), 4167–4171.
- (32) Feng, L.; Yuan, S.; Qin, J.-S.; Wang, Y.; Kirchon, A.; Qiu, D.; 658 Cheng, L.; Madrahimov, S. T.; Zhou, H.-C. Lattice Expansion and 659 Contraction in Metal-Organic Frameworks by Sequential Linker 660 Reinstallation. *Matter* **2019**, *1* (1), 156–167.
- (33) Xie, L.-H.; Liu, X.-M.; He, T.; Li, J.-R. Metal-Organic 662 Frameworks for the Capture of Trace Aromatic Volatile Organic 663 Compounds. *Chem.* **2018**, *4* (8), 1911–1927.
- (34) Gao, S.; Zhao, L.; Han, L.; Zhang, Z.; Zhao, H. Synthesis, 665 structure and characterization of two solvatochromic metal—organic 666 frameworks for chemical-sensing applications. *CrystEngComm* **2018**, 20 667 (16), 2237—2240.
- (35) Yu, L.; Wang, H.; Liu, W.; Teat, S. J.; Li, J. Blue-Light-Excitable, 669 Quantum Yield Enhanced, Yellow-Emitting, Zirconium-Based Metal—670 Organic Framework Phosphors Formed by Immobilizing Organic 671 Chromophores. Cryst. Growth Des. 2019, 19 (12), 6850—6854.
- (36) Kong, X.-J.; Zhang, Y.-Z.; He, T.; Wu, X.-Q.; Xu, M.-M.; Wang, 673 S.-N.; Xie, L.-H.; Li, J.-R. Two interpenetrated metal—organic 674 frameworks with a slim ethynyl-based ligand: designed for selective 675

- 676 gas adsorption and structural tuning. CrystEngComm 2018, 20 (39), 677 6018–6025.
- 678 (37) Xu, L.; Luo, Y.-P.; Sun, L.; Xu, Y.; Cai, Z.-S.; Fang, M.; Yuan, R.-679 X.; Du, H.-B. Highly Stable Mesoporous Zirconium Porphyrinic 680 Frameworks with Distinct Flexibility. *Chem. Eur. J.* **2016**, 22 (18), 681 6268–6276.
- 682 (38) Chen, C.-X.; Wei, Z.-W.; Cao, C.-C.; Yin, S.-Y.; Qiu, Q.-F.; Zhu, 683 N.-X.; Xiong, Y.-Y.; Jiang, J.-J.; Pan, M.; Su, C.-Y. All Roads Lead to 684 Rome: Tuning the Luminescence of a Breathing Catenated Zr-MOF by 685 Programmable Multiplexing Pathways. *Chem. Mater.* **2019**, *31* (15), 686 5550–5557.
- 687 (39) DeCoste, J. B.; Peterson, G. W. Metal—Organic Frameworks for 688 Air Purification of Toxic Chemicals. *Chem. Rev.* **2014**, *114* (11), 5695—689 5727.
- 690 (40) Islamoglu, T.; Chen, Z.; Wasson, M. C.; Buru, C. T.; Kirlikovali, 691 K. O.; Afrin, U.; Mian, M. R.; Farha, O. K. Metal—Organic Frameworks 692 against Toxic Chemicals. *Chem. Rev.* **2020**, *120* (16), 8130–8160.
- 693 (41) Liu, T.-F.; Vermeulen, N. A.; Howarth, A. J.; Li, P.; Sarjeant, A. 694 A.; Hupp, J. T.; Farha, O. K. Adding to the Arsenal of Zirconium-Based 695 Metal—Organic Frameworks: the Topology as a Platform for Solvent-696 Assisted Metal Incorporation. *Eur. J. Inorg. Chem.* **2016**, 2016 (27), 697 4349—4352.
- 698 (42) Wang, B.; Lv, X.-L.; Feng, D.; Xie, L.-H.; Zhang, J.; Li, M.; Xie, Y.; 699 Li, J.-R.; Zhou, H.-C. Highly Stable Zr(IV)-Based Metal—Organic 700 Frameworks for the Detection and Removal of Antibiotics and Organic 701 Explosives in Water. *J. Am. Chem. Soc.* **2016**, *138* (19), 6204–6216.
- 702 (43) Bumstead, A. M.; Cordes, D. B.; Dawson, D. M.; Chakarova, K. 703 K.; Mihaylov, M. Y.; Hobday, C. L.; Düren, T.; Hadjiivanov, K. I.; 704 Slawin, A. M. Z.; Ashbrook, S. E.; Prasad, R. R. R.; Wright, P. A. 705 Modulator-Controlled Synthesis of Microporous STA-26, an Inter-706 penetrated 8,3-Connected Zirconium MOF with the the-i Topology, 707 and its Reversible Lattice Shift. *Chem. Eur. J.* 2018, 24 (23), 6115—708 6126.
- (44) We induced the interpenetration of the NU-1200 MOF by 709 710 subjecting the non-interpenetrated activated framework to a solution of 711 DMF and formic acid at 120 °C. The decrease in pH due to the formic 712 acid, along with the addition of thermal energy to the system, leads to a 713 rapid interpretation process. We posit that the process begins with the 714 breaking of the coordination bonds between the hard acid \overline{Zr}^{4+} ions and 715 the hard base carboxylate oxygens of the tritopic TMTB linker by 716 protonation of the linker followed by a re-formation of the framework 717 when the MOF solution was placed in the oven at 120 °C. The formic 718 acid modulator may select for the thermodynamic product (STA-26) 719 over the kinetic product (NU-1200) by competing with the TMTB 720 ligands for the metal ions and protons in solution, which could slow the 721 self-assembly process. The decomposition of DMF at elevated 722 temperatures is also well-documented within the MOF literature and 723 produces methyl amine as the decomposition product, which can act as 724 a base to raise the p K_a of the solution and allow the free linker molecules 725 to re-form bonds to the Zr nodes in an interpenetrated fashion.
- 726 (45) Gong, X.; Gnanasekaran, K.; Chen, Z.; Robison, L.; Wasson, M. 727 C.; Bentz, K. C.; Cohen, S. M.; Farha, O. K.; Gianneschi, N. C. Insights 728 into the Structure and Dynamics of Metal—Organic Frameworks via 729 Transmission Electron Microscopy. *J. Am. Chem. Soc.* **2020**, 142 (41), 730 17224—17235.
- 731 (46) Moggach, S. A.; Bennett, T. D.; Cheetham, A. K. The Effect of 732 Pressure on ZIF-8: Increasing Pore Size with Pressure and the 733 Formation of a High-Pressure Phase at 1.47 GPa. *Angew. Chem., Int. Ed.* 734 **2009**, 48 (38), 7087–7089.
- 735 (47) Widmer, R. N.; Lampronti, G. I.; Chibani, S.; Wilson, C. W.; 736 Anzellini, S.; Farsang, S.; Kleppe, A. K.; Casati, N. P. M.; MacLeod, S. 737 G.; Redfern, S. A. T.; Coudert, F.-X.; Bennett, T. D. Rich Polymorphism 738 of a Metal—Organic Framework in Pressure—Temperature Space. *J. 739 Am. Chem. Soc.* **2019**, *141* (23), 9330—9337.
- 740 (48) Gagnon, K. J.; Beavers, C. M.; Clearfield, A. MOFs Under 741 Pressure: The Reversible Compression of a Single Crystal. *J. Am. Chem.* 742 Soc. **2013**, 135 (4), 1252–1255.
- 743 (49) Li, W.; Probert, M. R.; Kosa, M.; Bennett, T. D.; Thirumurugan, 744 A.; Burwood, R. P.; Parinello, M.; Howard, J. A. K.; Cheetham, A. K.

ı

- Negative Linear Compressibility of a Metal-Organic Framework. J. 745 Am. Chem. Soc. 2012, 134 (29), 11940-11943.
- (50) Tan, J. C.; Bennett, T. D.; Cheetham, A. K. Chemical structure, 747 network topology, and porosity effects on the mechanical properties of 748 Zeolitic Imidazolate Frameworks. *Proc. Natl. Acad. Sci. U. S. A.* **2010**, 749 107 (22), 9938–9943.
- (51) Redfern, L. R.; Farha, O. K. Mechanical Properties of Metal—751 Organic Frameworks. *Chem. Sci.* **2019**, *10* (46), 10666—10679.
- (52) Peterson, G. W.; DeCoste, J. B.; Glover, T. G.; Huang, Y.; Jasuja, 753 H.; Walton, K. S. Effects of Pelletization Pressure on the Physical and 754 Chemical Properties of the Metal—Organic Frameworks Cu₃(BTC)₂ 755 and UiO-66. *Microporous Mesoporous Mater.* **2013**, 179, 48–53.
- (53) Purewal, J. J.; Liu, D.; Yang, J.; Sudik, A.; Siegel, D. J.; Maurer, S.; 757 Müller, U. Increased Volumetric Hydrogen Uptake of MOF-5 by 758 Powder Densification. *Int. J. Hydrogen Energy* **2012**, 37 (3), 2723–759 2727.
- (54) Kitao, T.; Zhang, Y.; Kitagawa, S.; Wang, B.; Uemura, T. 761 Hybridization of MOFs and polymers. *Chem. Soc. Rev.* **2017**, 46 (11), 762 3108–3133.
- (55) Evans, J. D.; Fraux, G.; Gaillac, R.; Kohen, D.; Trousselet, F.; 764 Vanson, J.-M.; Coudert, F.-X. Computational Chemistry Methods for 765 Nanoporous Materials. *Chem. Mater.* **2017**, *29* (1), 199–212.
- (56) Le, S.-N.; Navrotsky, A. Energetics of formation of alkali and 767 ammonium cobalt and zinc phosphate frameworks. *J. Solid State Chem.* 768 **2008**, *181* (1), 20–29.
- (57) Trofymluk, O.; Levchenko, A. A.; Tolbert, S. H.; Navrotsky, A. 770 Energetics of Mesoporous Silica: Investigation into Pore Size and 771 Symmetry. *Chem. Mater.* **2005**, *17* (14), 3772–3783.
- (58) Hughes, J. T.; Bennett, T. D.; Cheetham, A. K.; Navrotsky, A. 773 Thermochemistry of Zeolitic Imidazolate Frameworks of Varying 774 Porosity. J. Am. Chem. Soc. 2013, 135 (2), 598–601.
- (59) Bennett, T. D.; Simoncic, P.; Moggach, S. A.; Gozzo, F.; Macchi, 776 P.; Keen, D. A.; Tan, J.-C.; Cheetham, A. K. Reversible pressure-777 induced amorphization of a zeolitic imidazolate framework (ZIF-4). 778 Chem. Commun. 2011, 47 (28), 7983–7985.
- (60) Widmer, R. N.; Lampronti, G. I.; Anzellini, S.; Gaillac, R.; 780 Farsang, S.; Zhou, C.; Belenguer, A. M.; Wilson, C. W.; Palmer, H.; 781 Kleppe, A. K.; Wharmby, M. T.; Yu, X.; Cohen, S. M.; Telfer, S. G.; 782 Redfern, S. A. T.; Coudert, F.-X.; MacLeod, S. G.; Bennett, T. D. 783 Pressure Promoted Low-Temperature Melting of Metal-Organic 784 Frameworks. *Nat. Mater.* 2019, 18 (4), 370–376.
- (61) Chapman, K. W.; Halder, G. J.; Chupas, P. J. Pressure-Induced 786 Amorphization and Porosity Modification in a Metal—Organic 787 Framework. J. Am. Chem. Soc. 2009, 131 (48), 17546—17547.
- (62) Yan, Y.; Juríček, M.; Coudert, F.-X.; Vermeulen, N. A.; Grunder, 789 S.; Dailly, A.; Lewis, W.; Blake, A. J.; Stoddart, J. F.; Schröder, M. Non-790 Interpenetrated Metal—Organic Frameworks Based on Copper(II) 791 Paddlewheel and Oligoparaxylene-Isophthalate Linkers: Synthesis, 792 Structure, and Gas Adsorption. J. Am. Chem. Soc. 2016, 138 (10), 793 3371–3381.
- (63) Oliver, W. C.; Pharr, G. M. Measurement of Hardness and Elastic 795 Modulus by Instrumented Indentation: Advances in Understanding 796 and Refinements to Methodology. *J. Mater. Res.* **2004**, *19* (1), 3–20. 797
- (64) Bobbitt, N. S.; Mendonca, M. L.; Howarth, A. J.; Islamoglu, T.; 798 Hupp, J. T.; Farha, O. K.; Snurr, R. Q. Metal—organic Frameworks for 799 The Removal of Toxic Industrial Chemicals and Chemical Warfare 800 Agents. Chem. Soc. Rev. 2017, 46 (11), 3357–3385.
- (65) Son, F. A.; Wasson, M. C.; Islamoglu, T.; Chen, Z.; Gong, X.; 802 Hanna, S. L.; Lyu, J.; Wang, X.; Idrees, K. B.; Mahle, J. J.; Peterson, G. 803 W.; Farha, O. K. Uncovering the Role of Metal—Organic Framework 804 Topology on the Capture and Reactivity of Chemical Warfare Agents. 805 Chem. Mater. 2020, 32 (11), 4609–4617.
- (66) Chen, H.; Snurr, R. Q. Understanding the Loading Dependence 807 of Adsorbate Diffusivities in Hierarchical Metal—Organic Frameworks. 808 *Langmuir* **2020**, 36 (5), 1372—1378.